

Sondheimer oscillations as a probe of non-ohmic flow in type-II Weyl semimetal WP2

Maarten van Delft (✉ maarten.vandelft@epfl.ch)

Institute of Materials (IMX), Ecole Polytechnique Federale de Lausanne (EPFL) <https://orcid.org/0000-0002-6952-9418>

Yaxian Wang

Harvard University

Carsten Putzke

Laboratory of Quantum Materials <https://orcid.org/0000-0002-6205-9863>

Jacopo Oswald

IBM Research

Georgios Varnavides

Harvard University

Christina Garcia

Harvard University <https://orcid.org/0000-0002-9259-3880>

Chunyu Guo

Ecole Polytechnique Federale de Lausanne (EPFL)

Heinz Schmid

IBM Research - Zurich <https://orcid.org/0000-0002-0228-4268>

Vicky Süß

Max Planck Institute for Chemical Physics of Solids

Horst Borrmann

Max Planck Institute for Chemical Physics of Solids <https://orcid.org/0000-0002-1397-3261>

Jonas Diaz

École Polytechnique Fédérale de Lausanne

Yan Sun

Max Planck Institute for Chemical Physics of Solids <https://orcid.org/0000-0002-7142-8552>

Claudia Felser

Max Planck Institute for Chemical Physics of Solids

Bernd Gotsmann

IBM Research - Zurich <https://orcid.org/0000-0001-8978-7468>

Prineha Narang

Harvard University <https://orcid.org/0000-0003-3956-4594>

Philip Moll

École Polytechnique Fédérale de Lausanne <https://orcid.org/0000-0002-7616-5886>

Article

Keywords: Non-ohmic Electron Flow, Electron Scattering, Conduction Regime, Magnetoresistance Oscillations, Momentum Exchange

Posted Date: February 11th, 2021

DOI: <https://doi.org/10.21203/rs.3.rs-131719/v1>

License:  This work is licensed under a Creative Commons Attribution 4.0 International License.

[Read Full License](#)

Version of Record: A version of this preprint was published at Nature Communications on August 10th, 2021. See the published version at <https://doi.org/10.1038/s41467-021-25037-0>.

1 Sondheimer oscillations as a probe of non-ohmic 2 flow in type-II Weyl semimetal WP₂

3 Maarten R. van Delft^{1,*}, Yaxian Wang², Carsten Putzke¹, Jacopo Oswald³, Georgios
4 Varnavides², Christina A. C. Garcia², Chunyu Guo¹, Heinz Schmid³, Vicky Süss⁴, Horst
5 Borrmann⁴, Jonas Diaz¹, Yan Sun⁴, Claudia Felser⁴, Bernd Gotsmann³, Prineha
6 Narang^{2,*}, and Philip J.W. Moll^{1,*}

7 ¹Laboratory of Quantum Materials (QMAT), Institute of Materials (IMX), École Polytechnique Fédérale de Lausanne
8 (EPFL), 1015 Lausanne, Switzerland

9 ²Harvard John A. Paulson School of Engineering and Applied Sciences, Harvard University, Cambridge, MA 02138,
10 USA.

11 ³IBM Research - Zurich, 8803 Rüschlikon, Switzerland

12 ⁴Max Planck Institute for Chemical Physics of Solids, Nöthnitzer Strasse 40, 01187 Dresden, Germany

13 *e-mail: maarten.vandelft@epfl.ch; prineha@seas.harvard.edu; philip.moll@epfl.ch

14 ABSTRACT

As conductors in electronic applications shrink, microscopic conduction processes lead to strong deviations from Ohm's law. Depending on the length scales of momentum conserving (l_{MC}) and relaxing (l_{MR}) electron scattering, and the device size (d), current flows may shift from ohmic to ballistic to hydrodynamic regimes and more exotic mixtures thereof. So far, an *in situ*, in-operando methodology to obtain these parameters self-consistently within a micro/nanodevice, and thereby identify its conduction regime, is critically lacking. In this context, we exploit Sondheimer oscillations, semi-classical magnetoresistance oscillations due to helical electronic motion, as a method to obtain l_{MR} in micro-devices even when $l_{MR} \gg d$. This gives
15 information on the bulk l_{MR} complementary to quantum oscillations, which are sensitive to all scattering processes. We extract l_{MR} from the Sondheimer amplitude in the topological semi-metal WP₂, at elevated temperatures up to $T \sim 50$ K, in a range most relevant for hydrodynamic transport phenomena. Our data on μm -sized devices are in excellent agreement with experimental reports of the large bulk l_{MR} and thus confirm that WP₂ can be microfabricated without degradation. Indeed, the measured scattering rates match well with those of theoretically predicted electron-phonon scattering, thus supporting the notion of strong momentum exchange between electrons and phonons in WP₂ at these temperatures. These results conclusively establish Sondheimer oscillations as a quantitative probe of l_{MR} in micro-devices in studying non-ohmic electron flow.

16 Main text

17 In macroscopic metallic wires, the flow of electric current is well described by Ohm's law, which assigns a metal a spatially-
18 uniform 'bulk' conductivity. The underlying assumption is that the complex and frequent scattering events of charge carriers
19 occur on the microscopic length scale of a mean-free-path, which is much smaller than the size of the conductor, d , leading to
20 diffusive behavior. In addition to the scattering processes of bulk systems, the resistance of microscopic conductors is mostly

21 dominated by boundary scattering, thereby masking the internal scattering processes of the bulk in resistance measurements.
22 Here, we present a method to uncover these bulk processes in micro-scale metals, which are of technological importance
23 for fabrication of quantum electronic devices, and simultaneously critical to a fundamental understanding of microscopic
24 current flow patterns. It is instructive to classify the bulk scattering processes into two categories: those that relax the electron
25 momentum, such as electron-phonon, Umklapp or inelastic scattering, occurring at length-scale l_{MR} ; and those that conserve
26 the electron momentum, such as direct or phonon-mediated electron-electron scattering, associated with a length scale l_{MC} .

27 Within a kinetic theory framework, these three length scales, namely d , l_{MR} , and l_{MC} , can be used to describe the current
28 flow in micro-scale conductors. When momentum-conserving interactions are negligible, ohmic flow at the macro-scale
29 ($l_{MC} \gg d \gg l_{MR}$) gives way to ballistic transport in clean metals where $l_{MR}, l_{MC} \gg d$. Conversely, when momentum-conserving
30 interactions occur over similar or smaller length scales to momentum-relaxing interactions, a third regime of ‘hydrodynamic’
31 transport ($l_{MR} \gg d \gg l_{MC}$) is observable^{1,2}. In this regime, the static transport properties of electron fluids can be described
32 by an effective viscosity that captures the momentum diffusion of the system^{2,3}. These electron fluids exhibit classical fluid
33 phenomena such as Poiseuille flow, whereby the current flow density is greatly decreased at the conductor boundary. Recently,
34 advances in both experimental probes and theoretical descriptions have enabled direct observation of these effects using
35 spatially-resolved current density imaging, and have hinted towards the rich landscape of electron hydrodynamics in micro-scale
36 crystals³⁻⁵.

37 While such local-probe experiments provide means of quantifying electron-electron interactions, and thus extracting l_{MC} ,
38 direct measurement of the intrinsic momentum-relaxing processes (l_{MR}) within micron-scale conductors remains elusive, yet is
39 greatly needed. From a practical perspective, l_{MR} describes the overall scattering from impurities and the lattice vibrations
40 within the metallic microstructure, which at low temperature is an important feedback parameter of quality control in fabrication.
41 Furthermore, given both the reduction of sample size and the improved crystal quality, seemingly exotic transport scenarios
42 where $l_{MR} \gg d \gg l_{MC}$ is satisfied are expected to become more prevalent in technology. An accurate description of these length
43 scales is necessary to predict the overall resistance and thus voltage drops and heat dissipation in the nanoelectronic devices. For
44 example, the resistive processes in a hydrodynamic conductor occur at the boundaries rather than homogeneously distributed in
45 the bulk, which alters the spatial distribution of Joule heating and thereby has significant impacts on thermal design.

46 Real devices will operate at some intermediate state in the d , l_{MR} , and l_{MC} parameter space, departing from the well-
47 understood limiting cases of ohmic, ballistic and hydrodynamic flow. Rich landscapes of distinct hydrodynamic transport
48 regimes are predicted depending on the relative sizes of the relevant length scales⁶. Effective understanding, modeling and
49 prediction of transport requires an experimental method to estimate these parameters reliably in every regime. In large,
50 ohmic conductors, the bulk mean-free-path l_{MR} can be simply estimated from the device resistance using a Drude model.
51 Yet when $l_{MC}, l_{MR} \gtrsim d$, boundary scattering dominates the resistance, and hence estimates of the bulk scattering parameters
52 are highly unreliable. This leaves the worrying possibility of misinterpreting the transport situation in a conductor, in that
53 the microfabrication itself may introduce defects or changes in the bulk properties that remain undetected by macroscopic
54 observables such as the resistance, but have profound impact on the microscopic current distribution. These effects are
55 already noticeable in state-of-the-art transistors, owing to the low carrier density of semi-conductors⁷, but have similarly been
56 reported in metallic conductors⁵. With the increased technological interest in quantum and classical electronics operating at
57 cryogenic temperatures, such questions about unconventional transport regimes are also of practical relevance in next generation

58 electronics⁸.

59 In this context, we propose to exploit a magneto-oscillatory phenomenon, Sondheimer oscillations (SO), as a self-consistent
60 method to obtain the transport scattering length l_{MR} *in-situ*, even in constricted channels when $l_{MR} \gg d$. In general, a magnetic
61 field (\vec{B}) applied perpendicular to a thin metal forces the carriers on the Fermi surface to undergo cyclotron motion. Those
62 on extremal orbits of the Fermi surface are localized in space due to the absence of a net velocity component parallel to the
63 magnetic field. These localized trajectories can become quantum-coherent, and their interference causes the well-known
64 Shubnikov-de Haas oscillations. The states away from extremal orbits also undergo cyclotron motion, yet they move with a net
65 velocity along the magnetic field, analogous to the helical trajectories of free electrons in a magnetic field (Fig. 1). These states
66 are responsible for the Sondheimer size effect which manifests itself as a periodic-in- B oscillation of the transport coefficients,
67 as discovered in the middle of the past century for clean elemental metals⁹.

68 For any given state, the magnitude of \vec{B} sets the helical radius and thus determines how many revolutions the electron
69 completes while travelling from one surface to the other in a microdevice. If an integer number of revolutions occur, the charge
70 carrier will have performed no net motion along the channel, and hence is semi-classically localized (Fig. 1a). However, if the
71 number of revolutions is non-integer, a net motion along the channel exists, delocalizing the carriers, resulting in oscillatory
72 magnetotransport behavior. Large-angle bulk scattering events dephase the trajectory, hence the strong sensitivity of SO to the
73 *bulk* l_{MR} even in nanostructures. These SO are an inherent property of mesoscale confined conductors in three dimensions and
74 have no counterpart in 2D metals like graphene.

75 The period of the SO is derived by considering a classical charged particle on a helical trajectory between two surfaces
76 perpendicular to the magnetic field¹⁰. One compares the time it takes to travel the distance d between the surfaces, $t_d = d/v_{\parallel}$,
77 to the time to complete a single cyclotron revolution, $\tau_c = 2\pi/\omega_c = 2\pi m^*/eB$ (m^* : effective mass, e : electron charge,
78 $\omega_c = eB/m^*$: cyclotron frequency). Their ratio describes the number of revolutions of the trajectory. For certain fields the
79 helix is commensurate with the finite structure and the number of revolutions is integer, n , such that $t_d = n\tau_c$. This occurs
80 periodically in field, with the period given by:

$$\Delta B = \frac{2\pi m^* v_{\parallel}}{ed} = \frac{\hbar}{ed} \left(\frac{\partial A}{\partial k_{\parallel}} \right). \quad (1)$$

81 The useful identity $v_{\parallel} = \frac{\hbar}{2\pi m^*} \left(\frac{\partial A}{\partial k_{\parallel}} \right)$, derived by Harrison¹¹, directly relates the SO period to the Fermi surface geometry, where
82 v_{\parallel} and k_{\parallel} denote the velocity and momentum component parallel to the magnetic field and A is the Fermi surface cross-sectional
83 area encircled by the orbit in k -space. Note the contrast to conventional quantum oscillations which appear around extremal
84 orbits, where $\frac{\partial A}{\partial k_{\parallel}} = 0$.

85 All conduction electrons undergo cyclotron motion, yet depending on $\frac{\partial A}{\partial k_{\parallel}}$, they experience different commensurability
86 fields with a structure of given size d . Hence oscillatory contributions to the total conductivity are washed out, unless a
87 macroscopic number of states share the same $v_{\parallel} \propto \left(\frac{\partial A}{\partial k_{\parallel}} \right)_{E_f}$ ¹⁰. In earlier days of Fermiology¹², geometric approximations
88 for Fermi surfaces, such as elliptical endpoints, were introduced to identify those generalized geometric features that lead
89 to extended regions of constant $\frac{\partial A}{\partial k_{\parallel}}$. The computational methods available nowadays allow a more modern approach to the
90 problem. Fermi surfaces calculated by ab-initio methods can be numerically sliced in order to calculate their cross-section
91 $A(k_{\parallel})$. We propose to extend this routine procedure, used to find extremal orbits relevant for quantum oscillations $\left(\frac{\partial A}{\partial k_{\parallel}} = 0 \right)$, to

92 identify SO-active regions $\left(\frac{\partial^2 A}{\partial k_{\parallel}^2} \sim 0\right)$, based on the Fermi-surface slicing code SKEAF¹³ (see the supplementary information
93 for details on implementation).

94 SO are caused by the real-space motion of charge carriers and hence also pose some conditions on the shape of the conductor.
95 First, surface scattering needs to be mostly diffusive. If an electron undergoes specular scattering N times before scattering
96 diffusively, it contributes towards the SO as if the sample had an effective thickness Nd ¹⁴, leading to overtones. Naturally, SO
97 vanish in the (unrealistic) limit of perfectly specular boundary conditions, as such ideal kinetic mirrors remove any interaction
98 of the electron system with the finite size of the conductor. Secondly, the conductor must feature two parallel, plane surfaces
99 perpendicular to the magnetic field to select only one spiral trajectory over the entire structure. The parallelicity requirement is
100 simply given by a fraction of the pitch of the spiral at a certain field ($\Delta d < v_{\parallel} \tau_c = d \frac{\Delta B}{B}$)¹⁰. These requirements are naturally
101 fulfilled in planar electronic devices.

102 It is instructive to briefly compare SO to the more widely known quantum oscillations of resistance, the Shubnikov-de Haas
103 effect (SdH). Both are probes of the Fermi surface geometry based on cyclotron orbits, yet the microscopies are strikingly
104 different. While quantum oscillation frequencies are exclusively determined by Fermi surface (FS) properties via the Onsager
105 relation and are thus independent of the sample shape, SO are finite-size effects. SO emerge from extended regions on the FS,
106 unlike SdH oscillations to which only states in close vicinity of extremal orbits contribute. While SdH oscillations are quantum
107 interference phenomena, SO are semi-classical, which is key to their use as a robust probe of exotic transport regimes. If both
108 can be observed, powerful statements on the scattering microscopies can be made, as SdH is sensitive to all dephasing collision
109 events and SO separates out the large-angle ones¹⁵. However, the much more stringent conditions of phase coherence in SdH
110 severely limit their observations at higher temperatures. SO are observable up to relatively high temperatures at which the
111 rapidly shrinking $l_{MR}(T)$ leads to a transition into an ohmic state, when $l_{MR}(T) < d$. As such, they are ideally suited to explore
112 the exotic transport regimes in which, for example, hydrodynamic effects occur.

113 We apply these theoretical considerations to experimentally investigate the scattering mechanisms in micron-sized crystalline
114 bars of the type-II Weyl semimetal WP₂¹⁶ exploiting the Sondheimer effect. Bulk single crystals of WP₂ are known for their
115 long l_{MR} , in the range of 100-500 μm ¹⁷⁻¹⁹, comparable to the elemental metals in which SO were initially discovered²⁰⁻²³.
116 These are an ideal test case for non-ohmic electron flow, as hydrodynamic transport signatures and nontrivial electron-phonon
117 dynamics have been observed in various topological semimetals^{17,18,24-26}. These ultra-pure crystals are then reduced in size by
118 nanofabrication techniques into constricted channels, to study hydrodynamic or ballistic corrections to the current flow.

119 Here we employ Focused Ion Beam (FIB) micromachining²⁷, which allows precise control over the channel geometry in
120 3D. In this technique, we accelerate Xe ions at 30 kV to locally sputter the target crystal grown by chemical vapor transport
121 (CVT)^{19,28} until a slab of desired dimensions in the μm -range remains. This technique leads to an amorphized surface of
122 around 10 nm thickness, yet has been shown to leave bulk crystal structures pristine²⁹. Naturally, reducing the size of a
123 conductor even without altering its bulk mean-free-path significantly changes the device resistance at low temperatures due
124 to finite size corrections³⁰. Hence, measurements of the constricted device resistance alone cannot exclude the possibility of
125 bulk degradation due to the fabrication step. Thus far, one could only argue based on size-dependent resistance studies that
126 the values smoothly extrapolate to the bulk resistivity value in the limit of infinite device size^{18,31}. Measuring SO directly
127 in the microfabricated devices themselves, however, quantitatively supports that the ultra-high purity of the parent crystal
128 remains unchanged by our fabrication. We note that the fundamental question of the bulk parameters is universal in mesoscopic

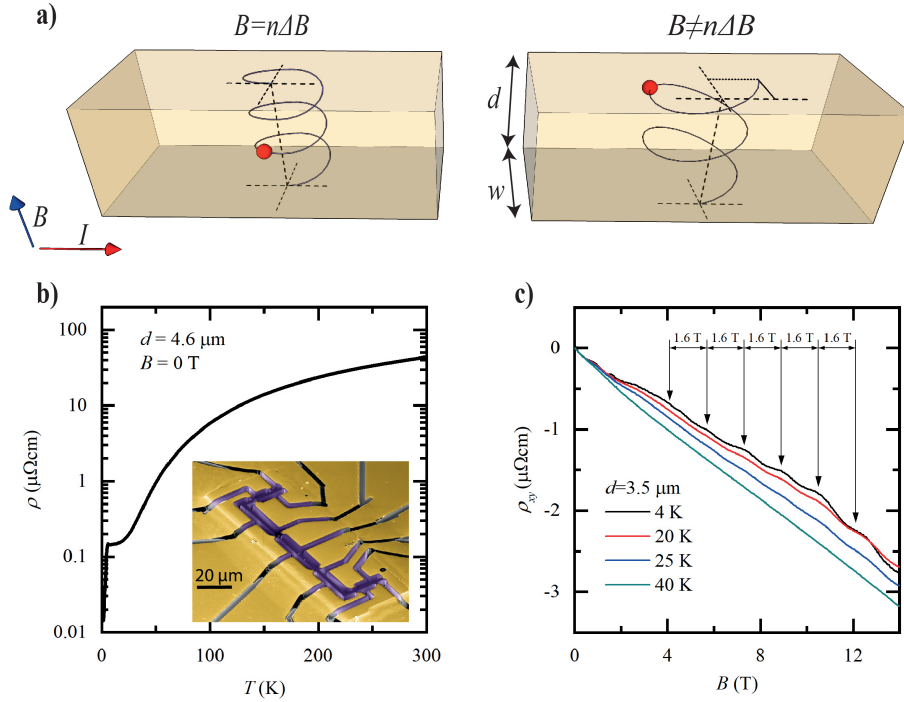


Figure 1. Introduction to Sondheimer oscillations. **a** Illustration of the Sondheimer effect. Left: the applied magnetic field is $B = 3\Delta B$ and the electron (red) makes an integer number of rotations, with no contribution to transport. Right: $B \neq n\Delta B$. The electron hits the top surface at a different position than its origin on the bottom surface, leading to a contribution to the conductivity. **b** Resistivity as function of temperature for a WP_2 microdevice. Inset: false-color SEM image of a typical device used in this study. **c** Sondheimer oscillations seen in the Hall resistivity of a WP_2 microdevice, for different temperatures. The oscillation period of $\Delta B = 1.6$ T is highlighted.

129 conducting structures irrespective of the fabrication technique, and these considerations are thus equally applicable to structures
 130 obtained by mechanically or chemically thinned samples as well as epitaxially grown crystalline films. SO should provide
 131 general insights into the material quality in the strongly confined regime, allowing to contrast different fabrication techniques.

132 At high temperatures, the resistivity measured in μm -confined devices agrees well with previous reports on high quality
 133 bulk crystals, as expected given the momentum relaxing limited mean-free-path of charge carriers in this regime (Fig. 1b). Yet
 134 in the low temperature limit, the device resistance exceeds those of bulk crystals by more than an order of magnitude^{17,19,32}.
 135 Conversely, the residual resistance ratios in our devices ($\text{RRR} \approx 160\text{-}300$) are also considerably lower than in bulk crystals³². The
 136 main question we address by SO is whether this excess resistance points to fabrication-induced damage, finite size corrections,
 137 or a mixture thereof. At low temperatures around 3 K, a drop in resistance signals a superconducting transition. As WP_2 in bulk
 138 form is not superconducting, this likely arises from an amorphous W-rich surface layer due to the FIB fabrication similar to
 139 observations made in NbAs ³³ and TaP ³⁴. In Fig. 1c, we show the Hall resistivity, ρ_{xy} , of one of our devices as a function of the
 140 magnetic field, for different temperatures. The Hall signal comprises oscillations with a period of $\Delta B = 1.6$ T, resolved above
 141 approximately $B=2$ T.

142 A hallmark signature of SO is their linear frequency dependence on the device thickness perpendicular to the field. For
 143 this reason, we fabricated crystalline devices with multiple sections of different thickness to study the d -dependence in a

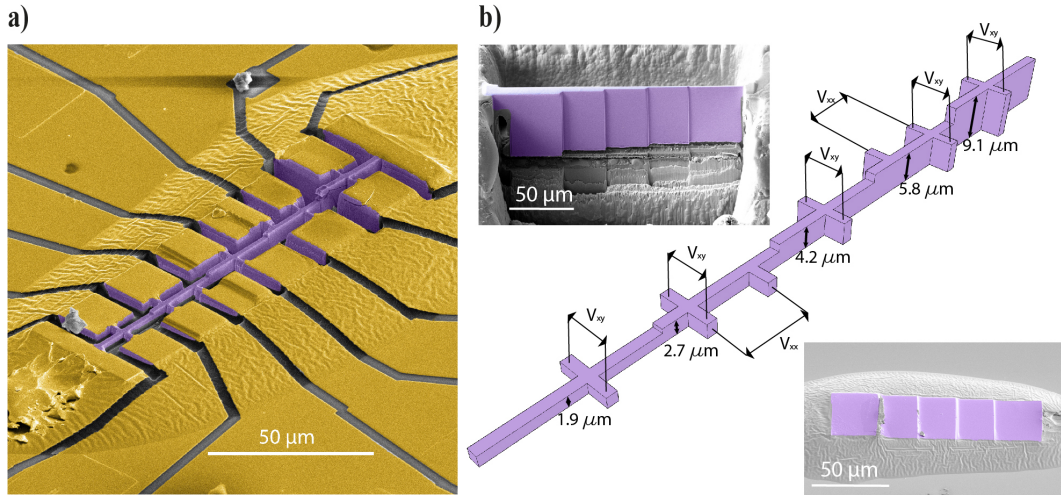


Figure 2. The staircase device. **a**, False color SEM image of a staircase device, used to measure Sondheimer oscillations for different thicknesses. The crystal is colored in purple, and gold contacts in yellow. **b**, Main: Schematic of the staircase device, illustrating all possible measurement configurations as well as the thickness of each section. Top left: SEM image of the lamella that will become the device shown in **a**, prior to extracting it from its parent crystal. Bottom right: SEM image of the same lamella, glued down onto a sapphire substrate, ready to define the device geometry. The lamella and glue are covered in gold (not colored) throughout the full field of view. The magnetic field is applied perpendicular to the structure, aligned along the crystallographic [011] direction.

144 consistent manner. This ‘staircase’ device allows the simultaneous measurement of transport on 5 steps of different thickness d ,
 145 as illustrated in Fig. 2. SO appear in all transport coefficients, magnetoresistance and Hall effect alike, yet here we focus on
 146 the Hall effect for two practical reasons. First, the step edges induce non-uniform current flows, and hence the device would
 147 need to be considerably longer to avoid spurious voltage contributions from currents flowing perpendicular to the device in a
 148 longitudinal resistance measurement. Second, WP_2 exhibits a very large magnetoresistance yet a small Hall coefficient, as
 149 typical for compensated semi-metals. Therefore, the SO are more clearly distinguishable against the background in a Hall
 150 measurement, but they are also present in the longitudinal channel (see Supplementary Information).

151 The fabrication process of our WP_2 devices follows largely the same procedure as described in Ref. 27. However, for the
 152 staircase device, a few key changes were made. In the first fabrication step, the FIB is used to cut a lamella from a bulk WP_2
 153 crystal. One side is polished flat, and the other side polished into five sections, each to a different thickness (Fig. 2b). It is then
 154 transferred, flat side down, into a drop of araldite epoxy on a sapphire substrate and electrically contacted by Au sputtering
 155 (Fig. 2b). In a second FIB step, the staircase slab is patterned laterally into its final structure (Fig. 2a).

156 All segments of the staircase devices show pronounced B -periodic oscillations in the Hall channel, from which the linear
 157 background is removed by taking second derivatives. (Fig. 3). At the lowest fields, a weak, aperiodic structure is observed. In
 158 this regime, the cyclotron diameter does not fit into the bar, preventing the formation of the Sondheimer spirals. Note that in all
 159 devices of different thickness, this onset field of the SO is the same. This is a natural consequence of the fact that the lateral
 160 size, perpendicular to the magnetic field, by design, is the same for all steps of the staircase. Each step, however, differs in
 161 thickness d parallel to the magnetic field, and the period varies accordingly between steps (Fig. 3b). At even higher fields, the

162 onset of regular SdH oscillations hallmarks a transition into a different quantized regime. The Sondheimer oscillation frequency
 163 $F = 1/\Delta B$ varies linearly with d as expected (Fig. 3c, Eq. 1).

164 Next we identify the Sondheimer-active region on the Fermi surface from the ab-initio band structure, which was calculated
 165 by density functional theory (DFT) with the projected augmented wave method as implemented in the code of the Vienna
 166 ab-initio Simulation Package (VASP)³⁵. The FS of WP₂ consists of two types of spin-split pockets: dogbone shaped electron
 167 pockets and extended cylindrical hole pockets (see Fig. 4 and supplementary Fig. S2 for a complete picture of the FS).

168 Only one area quantitatively agrees with the observed SO periodicity: the four equivalent endpoints of the dogbone (colored
 169 orange in Figs. 3f). Slicing all Fermi-surfaces using SKEAF¹³, their cross-sections $A(k_{\parallel})$ are obtained. While in quantum
 170 oscillation analysis this information is discarded once the extremal orbits are identified, it forms the basis of the SO analysis.
 171 As the dogbone is sliced from the endpoints, the area continuously grows until the two endpoint orbits merge and the area
 172 abruptly doubles. Slicing further, the area grows until the maximum orbit along the diagonal is reached. Inversion symmetry
 173 enforces then a symmetric spectrum when slicing further beyond the maximum. The quasi-linear growth at the endpoints
 174 signals an extended area of Sondheimer-active orbits. Averaging the near-constant derivative in this region, $\frac{\partial A}{\partial k_{\parallel}}$, provides via
 175 Eq. 1 a tuning-parameter-free prediction of the thickness dependence of the SO frequency. This ab-initio prediction (red line in
 176 Fig. 3c) is in excellent agreement with the observed thickness dependence.

177 Next the temperature-dependence of the SO amplitude is used to gain direct information about the microscopic scattering
 178 processes acting on this region of the Fermi surface. In Fig. 4a,b, we plot this temperature dependence and highlight two
 179 regimes: that of quantum coherence and that of purely Sondheimer oscillations. In the first regime, quantum coherence leads to
 180 SdH oscillations; however, for typical effective masses $m^* \approx m_e$, as in WP₂, they are only observable at very low temperatures
 181 ($T < 5$ K). Importantly, their quick demise upon increasing temperature is not driven by the temperature dependence of the
 182 scattering time, but rather by the broadening of the Fermi-Dirac distribution. This is apparent as their temperature dependence
 183 is well described by the Lifshitz-Kosevich formalism based on a temperature-independent quantum lifetime, τ_q .

184 This strong temperature-suppression of quantum oscillations severely limits their use to probe scattering mechanisms at
 185 elevated temperatures. SO, on the other hand, do not rely on quantum coherence and are readily observed to much higher
 186 temperatures, up to 50 K in WP₂, while their temperature decay allows a direct determination of the transport lifetime,
 187 $\tau_{MR} = l_{MR}/v_F$. Hence SO make an excellent tool to study materials in the temperature range pertinent to exotic transport
 188 regimes like ballistic or hydrodynamic. They self-evidence non-diffusive transport as they only vanish when $l_{MR} \sim d$, and
 189 hence are only absent in situations of conventional transport within a given device.

190 Key to observable SO is that electrons do not undergo large-angle scattering events on their path between the surfaces. We
 191 therefore have the condition that $l_{MR} > d$ ^{36,37}. As $l_{MR}(T)$ decreases with increasing temperature and the boundary scattering is
 192 assumed to be temperature-independent, the SO amplitude is suppressed as $e^{-d/l_{MR}(T)}$ which allows us to estimate the bulk
 193 transport mean-free-path within a finite-size sample, even when $d \ll l_{MR}$. It is extracted as³⁶:

$$\frac{1}{l_{MR}(T)} = -\frac{1}{d} \ln \frac{A(T)}{A(0)}, \quad (2)$$

194 where $A(T)$ is the SO amplitude at temperature T . $A(T = 0)$ is simply estimated by extrapolation, which is a robust procedure
 195 as the SO amplitude saturates at low but finite temperatures. This is analogous to the saturation of the resistivity of bulk metals

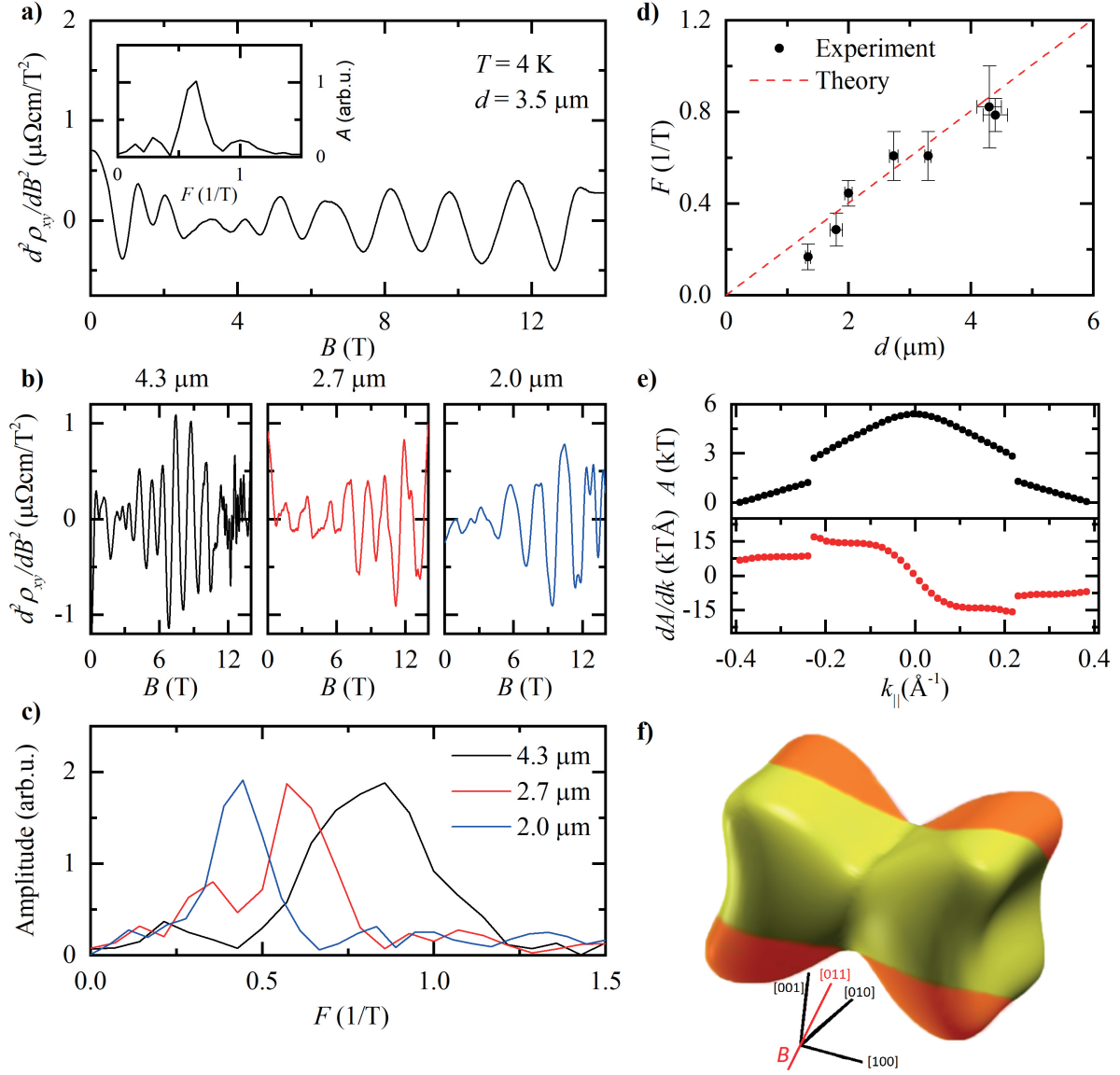


Figure 3. Analysis of Sondheimer oscillations in WP_2 . **a**, Second derivative of the Hall resistivity shown in Fig. 1c at $T = 4$ K. Inset: Fast Fourier Spectrum (FFT) corresponding to this data. **b**, Second derivatives of the Hall resistivity at three different thicknesses, $d = 4.3, 2.7$ and $2.0 \mu m$, $T = 4$ K. **c**, FFTs corresponding to the data in **b**. **d** Dependence of the Sondheimer frequency on d . The red dashed line is calculated from the Fermi surface as determined from DFT. **e** Cross-sectional area, A , of the dogbone Fermi surface pocket of WP_2 as a function of k parallel to the field direction of our experiments (top), and its derivative (bottom). **f** Location of observed Sondheimer orbits drawn on the dogbone-shaped Fermi surface pocket. The magnetic field is applied along the $[011]$ -direction, perpendicular to the current, as indicated by the red line.

196 at low temperatures, once bosonic scattering channels are frozen out and temperature-independent elastic defect scattering
 197 becomes dominant.

198 In the following discussion, we focus on the scattering time τ_{MR} to facilitate comparison of our results with literature
 199 and theory, using the average Fermi velocity on the dogbone Fermi surface determined from our band structure calculations

200 self-consistently, $v_F = 3.6 \times 10^5$ m/s. The $\tau_{MR}(T)$ obtained from all devices quantitatively agrees, despite their strong difference
 201 in thickness and hence SO frequency, further supporting the validity of this simple analysis (see Fig. 4c and Fig. S5). The
 202 lifetimes on the SO devices furthermore agree with measurements on bulk crystals¹⁸, evidencing that the increased resistivity
 203 compared to bulk can be wholly attributed to finite size corrections rather than to any fabrication-induced damage, and that
 204 FIB fabrication does not introduce significant changes to the bulk properties of WP₂ that might cause misinterpretations of the
 205 scattering regime.

206 For our WP₂ devices, a standard Dingle analysis¹⁵ of the quantum oscillations yields a quantum scattering time $\tau_q \sim$
 207 $10^{-13} - 10^{-12}$ s (Fig. 4c), in agreement with published values for bulk crystals WP₂¹⁹. As τ_q is sensitive to all dephasing
 208 scattering events, but τ_{MR} only to large-angle momentum relaxing scattering, the microscopics of the scattering processes in
 209 WP₂ are brought to light. The four orders of magnitude of difference between τ_{MR} and τ_q reflects a common observation in
 210 topological semi-metals such as Cd₃As₂³⁸, PtBi₂³⁹ or TaAs⁴⁰.

211 Long τ_{MR} , together with a high quality, clean sample, enables the realization of the hydrodynamic regime where the
 212 momentum conserving scattering dominates. These quantitative measurements of τ_q and $\tau_{MR}(T)$ can now be directly compared
 213 to theoretical models of scattering. We consider an initial electronic state with energy $\epsilon_{n\mathbf{k}}$ (where n and \mathbf{k} are the band index
 214 and wavevector respectively) scattering against a phonon with energy $\omega_{\mathbf{q}\nu}$ (where ν and \mathbf{q} are the phonon polarization and
 215 wavevector respectively), into a final electronic state with energy $\epsilon_{m\mathbf{k}+\mathbf{q}}$. The electron-phonon scattering time τ_{e-ph} describing
 216 such an interaction can be obtained from the electron self energy using Fermi's golden rule:

$$\tau_{\text{eph}}^{-1}(n\mathbf{k}) = \frac{2\pi}{\hbar} \sum_{m\nu} \int_{\text{BZ}} \frac{d\mathbf{q}}{\Omega_{\text{BZ}}} |g_{mn,\nu}(\mathbf{k}, \mathbf{q})|^2 \times \left(n_{\mathbf{q}\nu} + \frac{1}{2} \mp \frac{1}{2} \right) \delta(\epsilon_{n\mathbf{k}} \mp \omega_{\mathbf{q}\nu} - \epsilon_{m\mathbf{k}+\mathbf{q}}), \quad (3)$$

217 where Ω_{BZ} is the Brillouin zone volume, $f_{n\mathbf{k}}$ and $n_{\mathbf{q}\nu}$ are the Fermi-Dirac and Bose-Einstein distribution functions, respectively,
 218 and the electron-phonon matrix element for a scattering vertex is given by

$$g_{mn,\nu}(\mathbf{k}, \mathbf{q}) = \left(\frac{\hbar}{2m_0\omega_{\mathbf{q}\nu}} \right)^{1/2} \langle \psi_{m\mathbf{k}+\mathbf{q}} | \partial_{\mathbf{q}\nu} V | \psi_{n\mathbf{k}} \rangle. \quad (4)$$

219 Here $\langle \psi_{m\mathbf{k}+\mathbf{q}} |$ and $|\psi_{n\mathbf{k}} \rangle$ are Bloch eigenstates and $\partial_{\mathbf{q}\nu} V$ is the perturbation of the self-consistent potential with respect to ion
 220 displacement associated with a phonon branch with frequency $\omega_{\mathbf{q}\nu}$. Plotting these state-resolved electron-phonon lifetimes at
 221 ~ 10 K on the Fermi surface reveals the distribution of scattering in the SO-active regions (Fig. 4(d)). Equation 3, however,
 222 accounts, to first order, for all electron-phonon interactions, irrespective of the momentum transfer or equivalently the scattering
 223 angle. To remedy this, we augment the scattering rate with an 'efficiency' factor⁴² given by the relative change of the initial and
 224 final state momentum $(1 - \frac{v_{n\mathbf{k}} \cdot v_{n\mathbf{k}}}{|v_{n\mathbf{k}}||v_{n\mathbf{k}}|} = 1 - \cos \theta)$, where $v_{n\mathbf{k}}$ is the group velocity and θ is the scattering angle:

$$(\tau_{\text{eph}}^{\text{mr}}(n\mathbf{k}))^{-1} = \frac{2\pi}{\hbar} \sum_{m\nu} \int_{\text{BZ}} \frac{d\mathbf{q}}{\Omega_{\text{BZ}}} |g_{mn,\nu}(\mathbf{k}, \mathbf{q})|^2 \times \left(n_{\mathbf{q}\nu} + \frac{1}{2} \mp \frac{1}{2} \right) \delta(\epsilon_{n\mathbf{k}} \mp \omega_{\mathbf{q}\nu} - \epsilon_{m\mathbf{k}+\mathbf{q}}) \times \left(1 - \frac{v_{n\mathbf{k}} \cdot v_{n\mathbf{k}}}{|v_{n\mathbf{k}}||v_{n\mathbf{k}}|} \right). \quad (5)$$

225 At low temperatures, the thermally activated phonon modes have a tiny \mathbf{q} , therefore the initial and final electronic states only
 226 differ from a small angle. It is thus important to take this momentum-relaxation efficiency factor into account in addition to
 227 τ_{e-ph} , in order to estimate τ_{MR} which determines the electron mean free path in the SO-active regions. In the SO measurements,

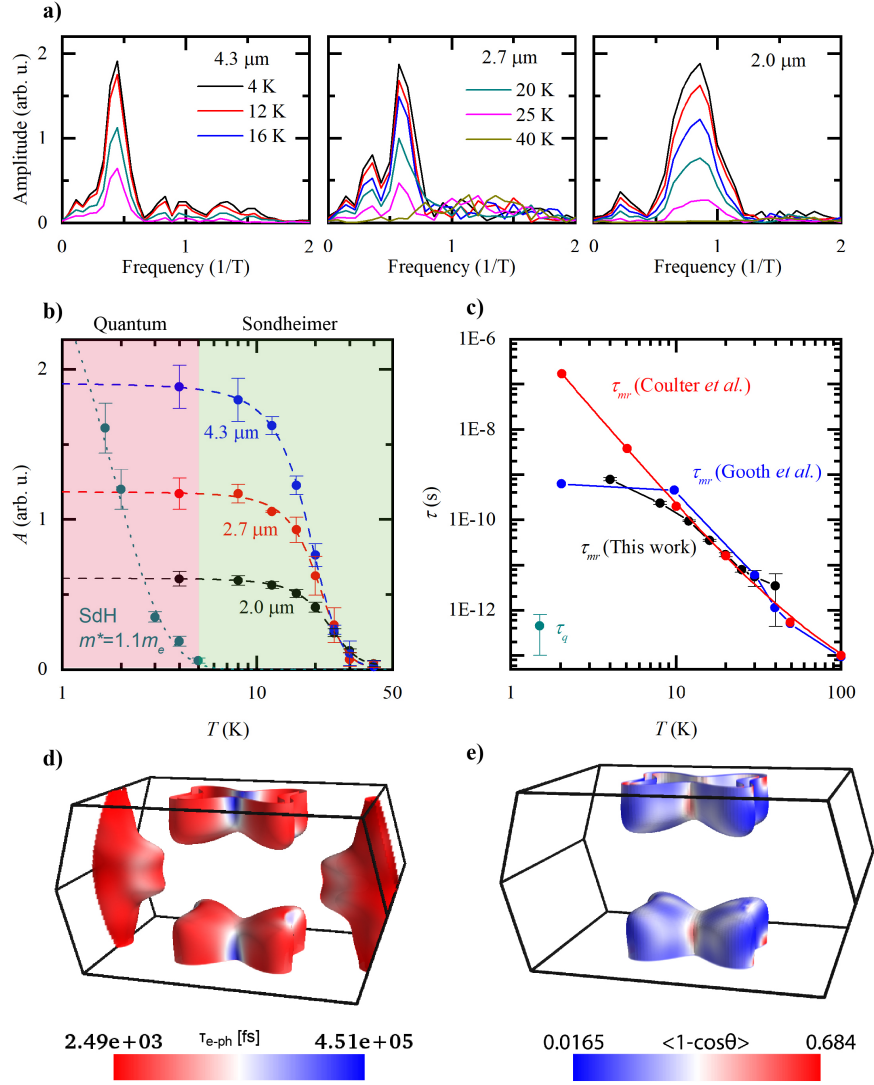


Figure 4. Extraction of scattering times from the Sondheimer amplitude. **a**, FFTs of the SO at different temperatures for thicknesses of 4.3, 2.7 and 2.0 μm . **b**, Temperature dependence of the Sondheimer and SdH oscillation amplitudes, for different sample thicknesses. The dashed lines are fits used to extrapolate to the amplitude at zero temperature, $A(0)$ (see the Supplementary Information for details). The dotted line is a Lifshitz-Kosevich fit, giving an effective mass of $1.1m_e$. Two regimes are highlighted: that of quantum coherence, where SdH oscillations exist alongside SO, and that of Sondheimer, where only SO exist. **c**, Scattering times extracted for WP_2 using Eq. 2 and the Fermi velocity from Ref. ¹⁸. An approximate quantum lifetime extracted from the SdH oscillations as well as data from Refs. ^{18,41} are included for comparison. **d** Calculated scattering time for all electron-phonon scattering ($\tau_{\text{e-ph}}$) and **e** the scattering efficiency determining the momentum-relaxing scattering lifetimes (τ_{MR}) projected onto the Fermi surface at $T=10$ K.

228 the electron orbits are located on the endpoints of the dogbone-shaped electron pockets (Fig. 3f), therefore we highlight
 229 the scattering efficiency distribution on the electron Fermi surface in Fig. 4e. Indeed, when the orbit is aligned along the diagonal
 230 direction, the Fermi surface cross section features very low scattering efficiency with an averaged $1 - \cos\theta < 0.1$. This supports
 231 our observation of frequently scattering electrons with long transport lifetimes in the SO measurement.

232 These results demonstrate the power of the Sondheimer size effect for the extraction of the momentum relaxing mean-
233 free-path in mesoscopic devices when $d \ll l_{MR}$ via their temperature dependence. Combined with first-principles theoretical
234 calculations we were able to locate the states contributing to the helical motion to the elliptical endpoints of a particular Fermi
235 surface of WP_2 . We note however that such analysis as well as the thickness dependence are only relevant for the academic
236 purpose of robustly identifying these oscillations as SO. Once this is established, the relevant lifetimes may straightforwardly
237 be obtained from the resistance oscillations at a single thickness. Hence, Sondheimer oscillations promise to be a powerful
238 probe to obtain the bulk mean-free-path in devices with μm -scale dimensions without relying on any microscopic model
239 assumptions. This analysis is a clear pathway to identify scattering processes in clean conductors within operating devices. It
240 thereby provides important feedback of the materials quality at and after a micro-/nano-fabrication procedure and disentangles
241 the roles of bulk and surface scattering that are inseparably intertwined in averaged transport quantities of strongly confined
242 conductors, such as the resistance. As their origin is entirely semi-classical, they are not restricted by stringent criteria such as
243 quantum coherence and thus span materials parameters of increased scattering rate. In particular, they survive up to significantly
244 higher temperatures and thereby allow microscopic spectroscopy in new regimes of matter dominated by strong quasiparticle
245 interactions, such as hydrodynamic electron transport. With this quantitative probe, it will be exciting to test recent proposals of
246 exotic transport regimes and create devices that leverage such unconventional transport in quantum materials.

247 References

- 248 1. Zaanen, J. Electrons go with the flow in exotic material systems. *Science* **351**, 1026–1027, (2016).
- 249 2. Levitov, L. & Falkovich, G. Electron viscosity, current vortices and negative nonlocal resistance in graphene. *Nat. Phys.*
250 **12**, 672–676, (2016).
- 251 3. Varnavides, G., Jermyn, A. S., Anikeeva, P., Felser, C. & Narang, P. Electron hydrodynamics in anisotropic materials. *Nat.*
252 *Commun.* **11**, 4710 (2020).
- 253 4. Sulpizio, J. A. *et al.* Visualizing Poiseuille flow of hydrodynamic electrons. *Nature* **576**, 75–79 (2019).
- 254 5. Vool, U. *et al.* Imaging phonon-mediated hydrodynamic flow in WTe_2 with cryogenic quantum magnetometry. *ArXiv*
255 2009.04477 (2020).
- 256 6. Gurzhi, R. N., Kalinenko, A. N. & Kopeliovich, A. I. Hydrodynamic effects in the electrical conductivity of impure metals.
257 *Zh. Eksp. Teor. Fiz.* **96**, 1522–1532 (1989).
- 258 7. Bufler, F. M. *et al.* Monte Carlo simulation and measurement of nanoscale n-MOSFETs. *IEEE Transactions on Electron*
259 *Devices* **50**, 418–424 (2003).
- 260 8. Jazaeri, F., Beckers, A., Tajalli, A. & Sallese, J. M. A review on quantum computing: Qubits, cryogenic electronics and
261 cryogenic MOSFET physics. *Proc. of the 26th international conference "Mixed design of integrated circuits and systems"*
262 (2019).
- 263 9. Sondheimer, E. H. The influence of a transverse magnetic field on the conductivity of thin metallic films. *Phys. Rev.* **80**,
264 401–406 (1950).
- 265 10. Gurevich, V. L. Oscillations in the conductivity of metallic films in magnetic field. *Sov. Phys. JETP* **35(8)**, 464–470 (1959).

- 266 **11.** Harrison, W. A. Electronic structure of polyvalent metals. *Phys. Rev.* **118**, 1190–1208 (1960).
- 267 **12.** Hambourger, P. D. & Marcus, J. A. Size-dependent oscillatory magnetoresistance in cadmium. *Phys. Rev. B* **8**, 5567–5578
268 (1973).
- 269 **13.** Rourke, P. M. & Julian, S. R. Numerical extraction of de Haas–van Alphen frequencies from calculated band energies.
270 *Comput. Phys. Commun.* **183**, 324–332 (2012).
- 271 **14.** Mackey, H. J. & Sybert, J. R. Harmonic content of magnetomorphic oscillations in the kinetic coefficients of electron
272 transport due to partially specular boundary scattering. *Phys. Rev.* **158**, 658–661 (1967).
- 273 **15.** Shoenberg, D. *Magnetic oscillations in metals* (Cambridge University Press, 1984).
- 274 **16.** Autès, G., Gresch, D., Troyer, M., Soluyanov, A. A., Yazyev, O. V., Robust Type-II Weyl Semimetal Phase in Transition
275 Metal Diphosphides XP_2 ($X=Mo, W$). *Phys. Rev. Lett.* **117**, 066402 (2016).
- 276 **17.** Jaoui, A. *et al.* Departure from the Wiedemann–Franz law in WP_2 driven by mismatch in T-square resistivity prefactors.
277 *npj Quantum Mater.* **3**, 64 (2018).
- 278 **18.** Gooth, J. *et al.* Thermal and electrical signatures of a hydrodynamic electron fluid in tungsten diphosphide. *Nat. Commun.*
279 **9**, 4093 (2018).
- 280 **19.** Kumar, N. *et al.* Extremely high magnetoresistance and conductivity in the type-II Weyl semimetals WP_2 and MoP_2 . *Nat.*
281 *Commun.* **8**, 1642 (2017).
- 282 **20.** Grishin, A., Lutsishin, P., Ostroukhov, Y. & Panchenko, O. Multiple Sondheimer oscillations in tungsten plates with
283 atomically pure surfaces. *Sov. J. Exp. Theor. Phys.* **49**, 673 (1979).
- 284 **21.** Alstadheim, T. & Risnes, R. Sondheimer oscillations in aluminium single crystals. *Philos. Mag.* **18**, 885–894 (1968).
- 285 **22.** Kunzler, J. E. & Renton, C. A. "Size effect" in electrical resistivity measurements on single crystals of high-purity tin at
286 liquid helium temperatures. *Phys. Rev.* **108**, 1397 (1957).
- 287 **23.** Babiskin, J. & Siebenmann, P. G. New type of oscillatory magnetoresistance in metals. *Phys. Rev.* **107**, 1249–1254 (1957).
- 288 **24.** Coulter, J. *et al.* Uncovering electron-phonon scattering and phonon dynamics in type-I Weyl semimetals. *Phys. Rev. B*
289 **100**, 220301(R) (2019).
- 290 **25.** Narang, P., Garcia, C. A. & Felser, C. The topology of electronic band structures. *Nat. Mater.* (2020).
- 291 **26.** Osterhoudt, G. B. *et al.* Evidence for dominant phonon-electron scattering in Weyl semimetal WP_2 . *ArXiv*, 2007.10364
292 (2020).
- 293 **27.** Moll, P. J. Focused ion beam microstructuring of quantum matter. *Annu. Rev. Condens. Matter Phys.* **9**, 147–162 (2018).
- 294 **28.** Shekhar, C. *et al.* Single crystal growth for topology and beyond. *Chem. Met. Sci. & Solid State Chem.* (2018).
- 295 **29.** Kelley, R., Song, K., Van Leer, B., Wall, D. & Kwakman, L. Xe+ FIB milling and measurement of amorphous silicon
296 damage. *Microsc. Microanal.* **19**, 862–863 (2013).
- 297 **30.** Fuchs, K. The conductivity of thin metallic films according to the electron theory of metals. *Math. Proc. Camb. Philos.*
298 *Soc.* **34**, 100–108 (1938).

- 299 **31.** Moll, P. J. W., Kushwaha, P., Nandi, N., Schmidt, B. & Mackenzie, A. P. Evidence for hydrodynamic electron flow in
300 PdCoO₂. *Science* **351** (2016).
- 301 **32.** Schönemann, R. *et al.* Fermi surface of the Weyl type-II metallic candidate WP₂. *Phys. Rev. B* **96**, 121108(R) (2017).
- 302 **33.** Bachmann, M. D. *et al.* Inducing superconductivity in Weyl semi-metal microstructures by selective ion sputtering. *Sci.*
303 *Adv.* **3**, e1602983 (2017). 288
- 304 **34.** Van Delft, M. R. *et al.* Two- and three-dimensional superconducting phases in the Weyl semimetal TaP at ambient pressure.
305 *Crystals* **10**, 288 (2020).
- 306 **35.** Kresse, G. & Furthmüller, J. Efficiency of ab-initio total energy calculations for metals and semiconductors using a
307 plane-wave basis set. *Comput. Mater. Sci.* **6**, 15–50 (1996).
- 308 **36.** Sato, H. Phonon-limited mean free path in the Sondheimer oscillation of aluminum. *J. Low Temp. Phys.* **38**, 267–275
309 (1980).
- 310 **37.** Munarin, J. A., Marcus, J. A. & Bloomfield, P. E. Size-dependent oscillatory magnetoresistance effect in gallium. *Phys.*
311 *Rev.* **172**, 718–736 (1968).
- 312 **38.** Liang, T. *et al.* Ultrahigh mobility and giant magnetoresistance in Cd₃As₂: protection from backscattering in a Dirac
313 semimetal. *Nat. Mater.* **14**, (2014).
- 314 **39.** Gao, W. *et al.* Extremely large magnetoresistance in a topological semimetal candidate pyrite PtBi₂. *Phys. Rev. Lett.* **118**,
315 256601 (2017).
- 316 **40.** Zhang, C. L. *et al.* Electron scattering in tantalum monoarsenide. *Phys. Rev. B* **95**, 085202 (2017).
- 317 **41.** Coulter, J., Sundararaman, R. & Narang, P. Microscopic origins of hydrodynamic transport in the type-II Weyl semimetal
318 WP₂. *Phys. Rev. B* **98**, 115130 (2018).
- 319 **42.** Ziman, J. M. *Electrons and phonons: the theory of transport phenomena in solids* (Oxford University Press, 2001).

320 Acknowledgements

321 M.R.v.D. acknowledges funding from the Rubicon research program with project number 019.191EN.010, which is financed by
322 the Dutch Research Council (NWO). This project was funded by the European Research Council (ERC) under the European
323 Union's Horizon 2020 research and innovation program (grant no. 715730, MiTopMat). Y.W. is partially supported by the
324 STC Center for Integrated Quantum Materials, NSF Grant No. DMR-1231319 for development of computational methods
325 for topological materials. This research used resources of the National Energy Research Scientific Computing Center, a DOE
326 Office of Science User Facility supported by the Office of Science of the U.S. Department of Energy under Contract No.
327 DE-AC02-05CH11231 as well as resources at the Research Computing Group at Harvard University. P.N. is a Moore Inventor
328 Fellow and gratefully acknowledges support through Grant No. GBMF8048 from the Gordon and Betty Moore Foundation.
329 C.A.C.G. acknowledges support from the NSF Graduate Research Fellowship Program under Grant No. DGE-1745303. We
330 acknowledge financial support from DFG through SFB 1143 (project-id 258499086) and the Würzburg-Dresden Cluster 274 of
331 Excellence on Complexity and Topology in Quantum Matter – ct.qmat (EXC 2147, project-id 39085490). B.G. acknowledges
332 financial support from the Swiss National Science Foundation (grant number CRSII5_189924). H.S and B.G thank J. Gooth for

333 discussion and K. Moselund, S. Reidt, and A. Molinari for support, and received funding from the European Union's Horizon
334 2020 research and innovation program under Grant Agreement ID 829044 "SCHINES".

335 **Author contributions**

336 MRvD, CP, JO, CG, JD performed the transport experiments, as well as the microfabrication in collaboration with BG and HS.
337 The crystals were grown by VS and CF, and crystallographically analyzed by HB. YS and CF calculated the band structures, and
338 YW, GV, CACG, PN performed the electron-phonon scattering calculations. BG, CF, PN and PJWM conceived the experiment,
339 and all authors contributed to writing of the manuscript.

340 **Competing interests**

341 The authors declare no competing financial interest.

342 **Supplementary information**

343

Figures

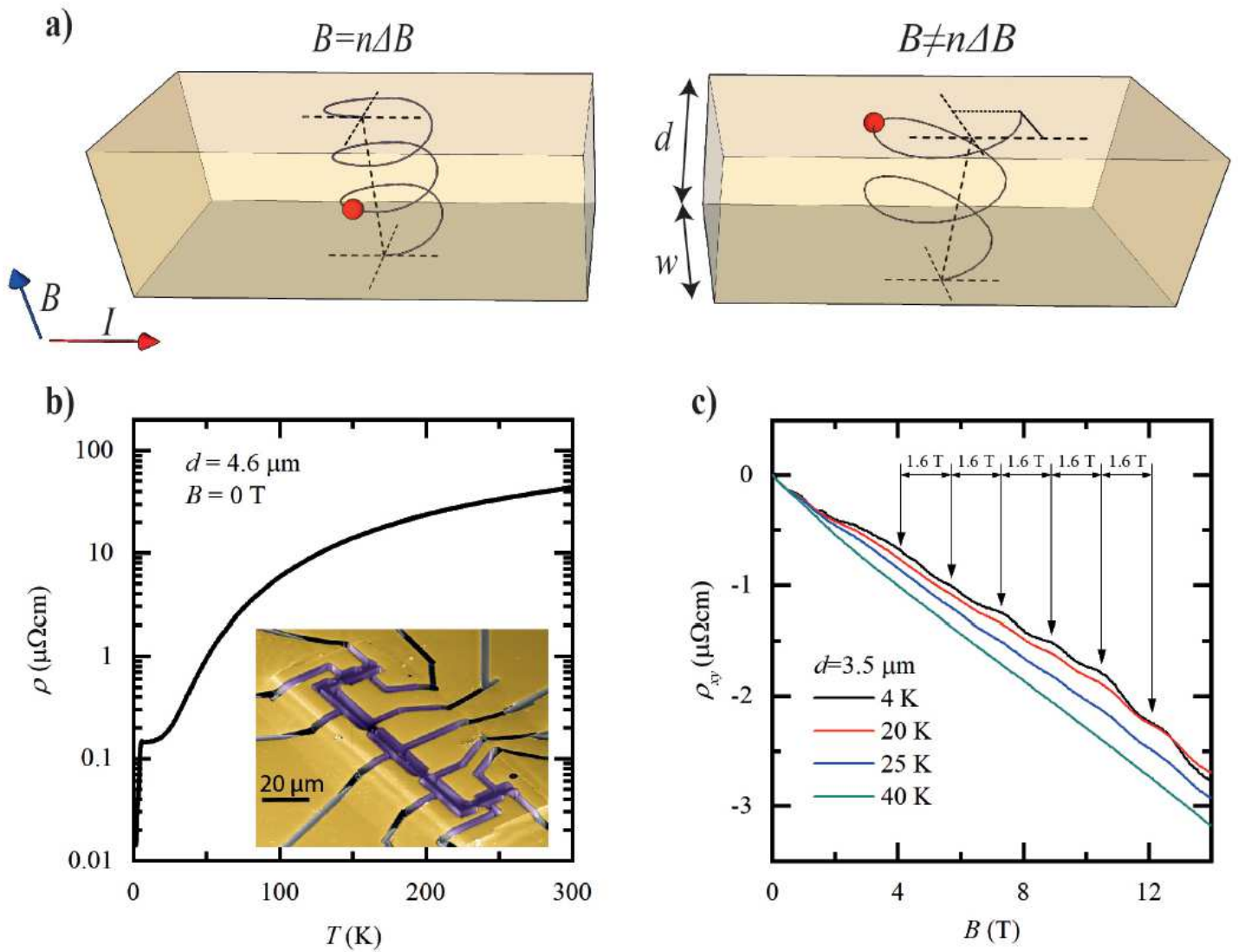


Figure 1

Introduction to Sondheimer oscillations. a Illustration of the Sondheimer effect. Left: the applied magnetic field is $B = 3\Delta B$ and the electron (red) makes an integer number of rotations, with no contribution to transport. Right: $B \neq n\Delta B$. The electron hits the top surface at a different position than its origin on the bottom surface, leading to a contribution to the conductivity. b Resistivity as function of temperature for a WP2 microdevice. Inset: false-color SEM image of a typical device used in this study. c Sondheimer oscillations seen in the Hall resistivity of a WP2 microdevice, for different temperatures. The oscillation period of $\Delta B = 1.6 \text{ T}$ is highlighted.

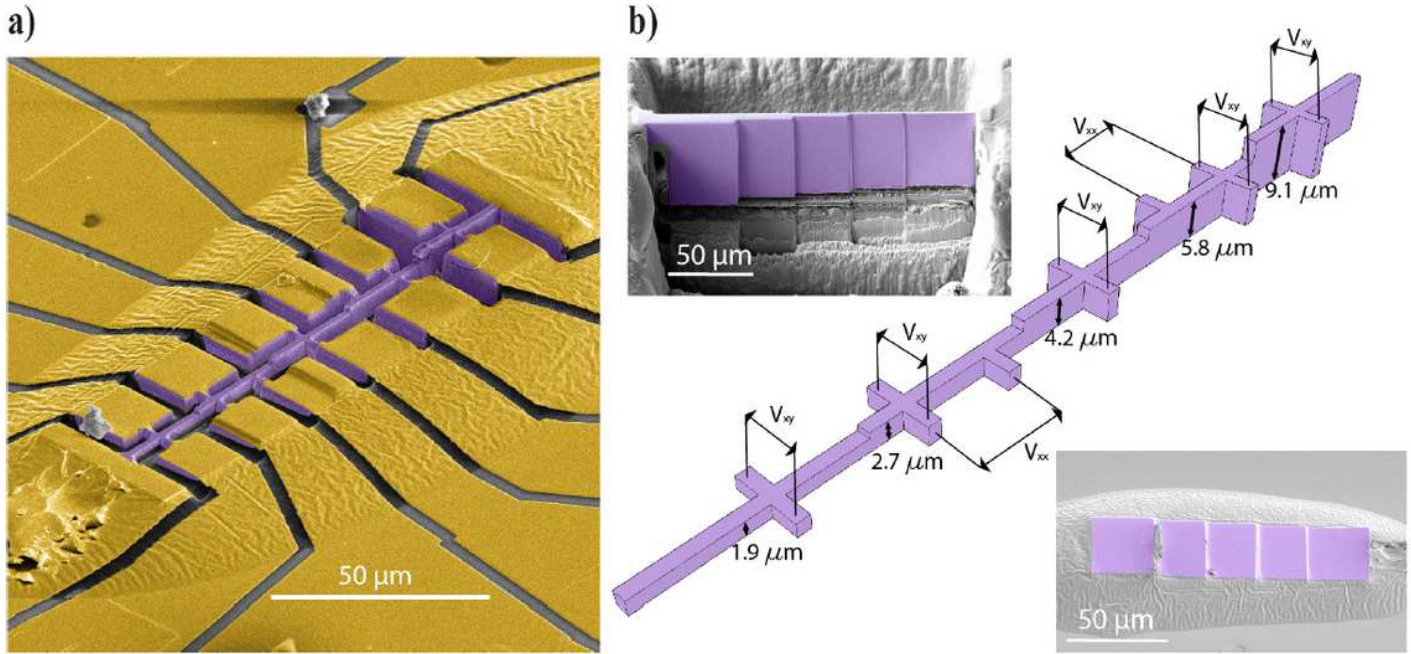


Figure 2

The staircase device. a, False color SEM image of a staircase device, used to measure Sondheimer oscillations for different thicknesses. The crystal is colored in purple, and gold contacts in yellow. b, Main: Schematic of the staircase device, illustrating all possible measurement configurations as well as the thickness of each section. Top left: SEM image of the lamella that will become the device shown in a, prior to extracting it from its parent crystal. Bottom right: SEM image of the same lamella, glued down onto a sapphire substrate, ready to define the device geometry. The lamella and glue are covered in gold (not colored) throughout the full field of view. The magnetic field is applied perpendicular to the structure, aligned along the crystallographic [011] direction.

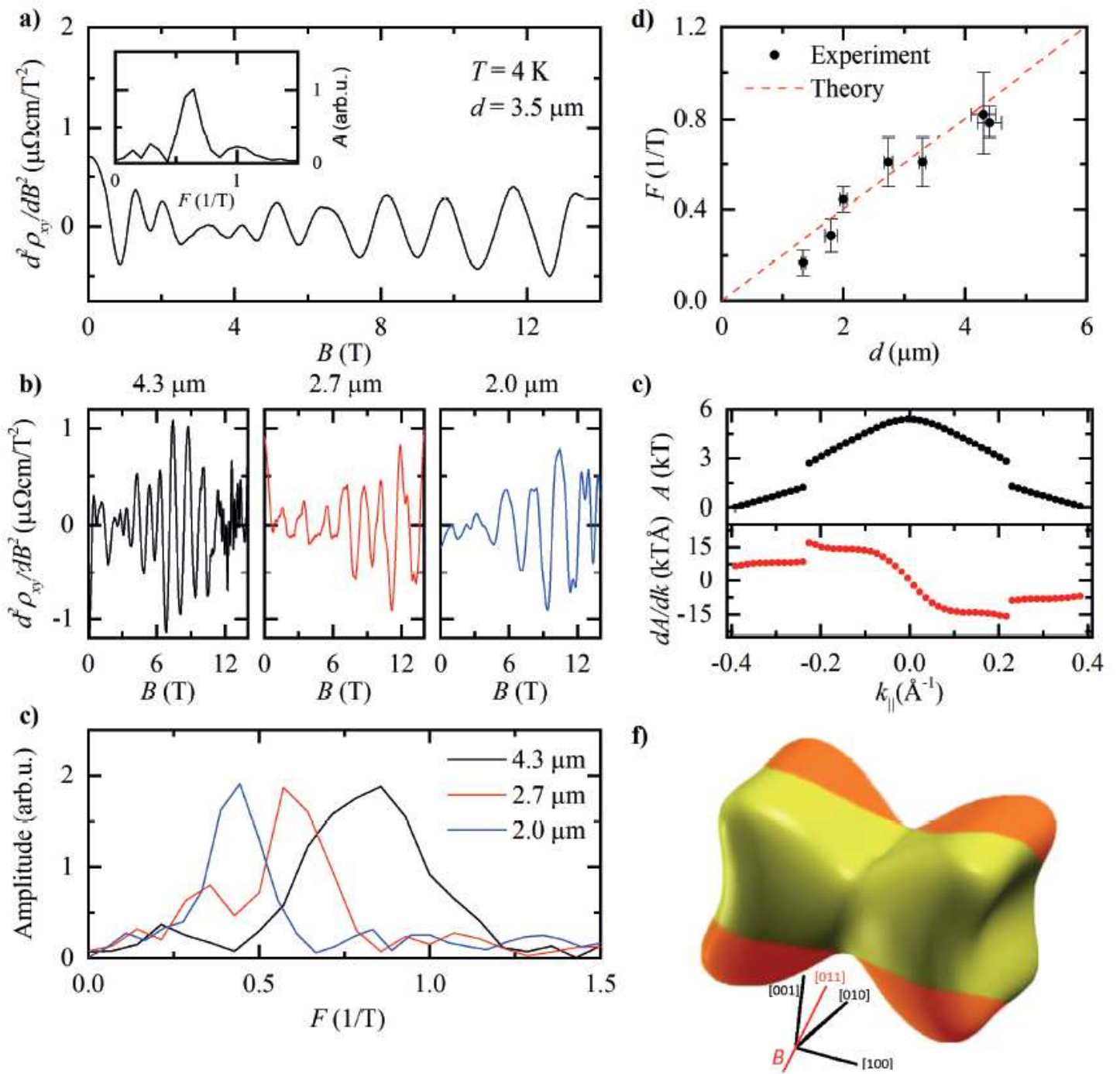


Figure 3

Analysis of Sondheimer oscillations in WP2. a, Second derivative of the Hall resistivity shown in Fig.1c at $T = 4$ K. Inset: Fast Fourier Spectrum (FFT) corresponding to this data. b, Second derivatives of the Hall resistivity at three different thicknesses, $d = 4.3, 2.7$ and $2.0 \mu\text{m}$, $T = 4$ K. c, FFTs corresponding to the data in b. d Dependence of the Sondheimer frequency on d . The red dashed line is calculated from the Fermi surface as determined from DFT. e Cross-sectional area, A , of the dogbone Fermi surface pocket of WP2 as a function of k parallel to the field direction of our experiments (top), and its derivative (bottom). f Location of observed Sondheimer orbits drawn on the dogbone-shaped Fermi surface pocket. The

magnetic field is applied along the [011]-direction, perpendicular to the current, as indicated by the red line.

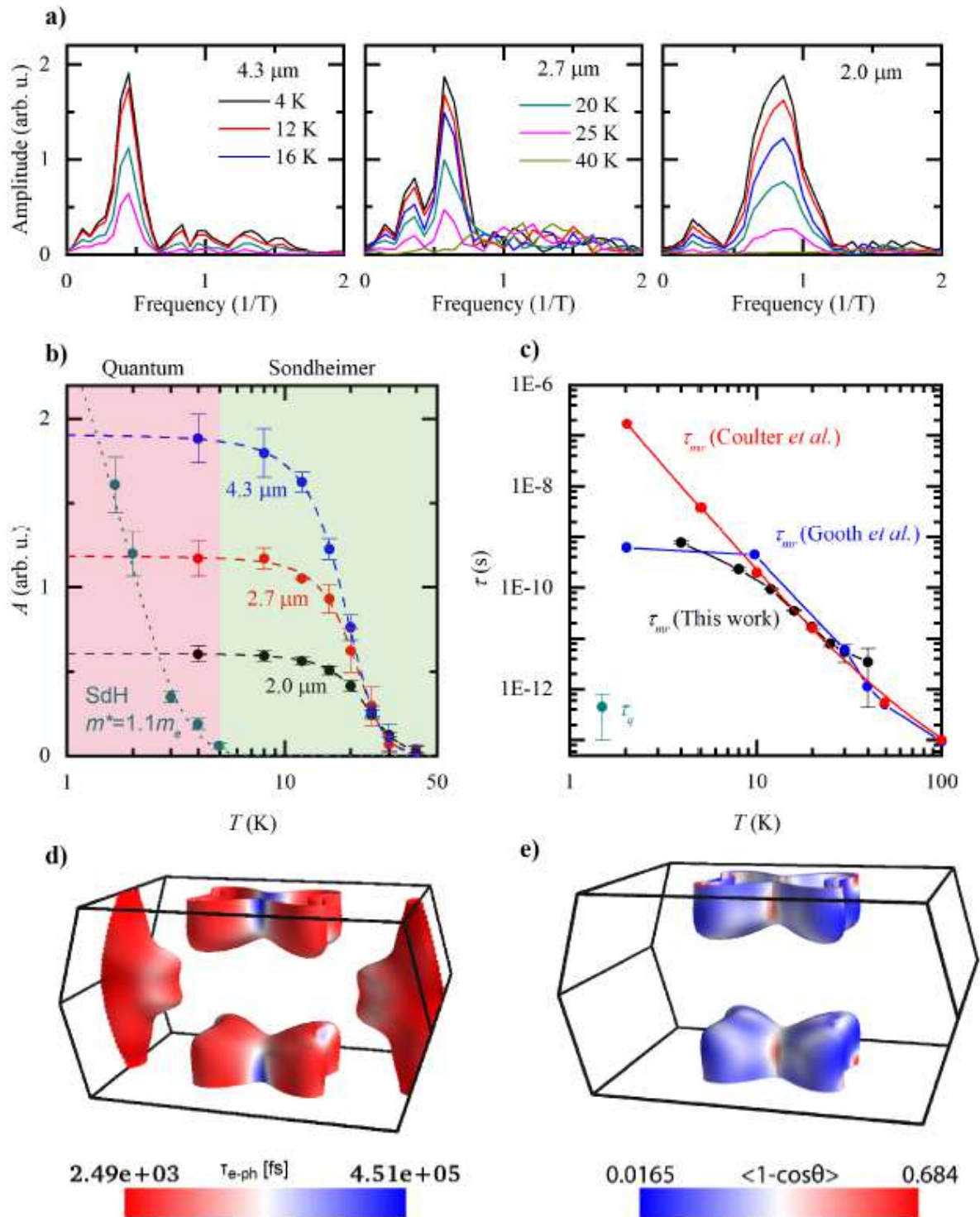


Figure 4

Extraction of scattering times from the Sondheimer amplitude. a, FFTs of the SO at different temperatures for thicknesses of 4.3, 2.7 and 2.0 μm . b, Temperature dependence of the Sondheimer and SdH oscillation amplitudes, for different sample thicknesses. The dashed lines are fits used to

extrapolate to the amplitude at zero temperature, $A(0)$ (see the Supplementary Information for details). The dotted line is a Lifshitz-Kosevich fit, giving an effective mass of $1.1m_e$. Two regimes are highlighted: that of quantum coherence, where SdH oscillations exist alongside SO, and that of Sondheimer, where only SO exist. c, Scattering times extracted for WP2 using Eq. 2 and the Fermi velocity from Ref.18. An approximate quantum lifetime extracted from the SdH oscillations as well as data from Refs.18, 41 are included for comparison. d Calculated scattering time for all electron-phonon scattering (τ_{e-ph}) and e the scattering efficiency determining the momentum-relaxing scattering lifetimes (τ_{MR}) projected onto the Fermi surface at $T = 10$ K.

Supplementary Files

This is a list of supplementary files associated with this preprint. Click to download.

- [Supplementaryinformation.pdf](#)